ACS APPLIED NANO MATERIALS

www.acsanm.org
Article

Ethyl Acetate Detection Using Mixed-Phase In_2O_3 Nanorods

Gustavo Sanghikian Marques dos Santos, Reinaldo dos Santos Theodoro, Gabriela Oliveira Gera, Tarcísio Micheli Perfecto, and Diogo Paschoalini Volanti*

Cite This: *ACS Appl. Nano Mater.* 2025, 8, 11458−11469

ABSTRACT: Detecting microbial volatile organic compounds (MVOCs) is critical for public health and food quality control applications but often requires complex analytical approaches. Ethyl acetate, an MVOC produced during the fermentation of bread and beer by *Saccharomyces cerevisiae*, holds significance in food quality control. Semiconductor metal oxides, particularly In_2O_3, are promising materials for MVOC sensing due to their cost-effectiveness, stability, and tunable sensing properties at the nanoscale. Enhanced sensing performance can be achieved by engineering heterostructures combining cubic and rhombohedral phases of In_2O_3 nanorods. In this work, In_2O_3 nanorods were synthesized via microwave-assisted hydrothermal method followed by calcination at 600, 500, and 400 °C to obtain single-phase cubic (In_2O_3-600) and mixed-phase cubic-rhombohedral (In_2O_3-500 and In_2O_3-400) structures. The In_2O_3-500 heterostructure nanorods exhibited an enhanced response of 548 to ethyl acetate at 350 °C in dry air. It also showed a fast response time (1.8 s), a selectivity ratio of 2.1, and a theoretical detection limit of 525 ppb. Moreover, the material maintained a high response under 90% relative humidity (RH), demonstrating robustness under realistic operating conditions. These findings can be attributed to the synergistic effect of heterojunctions formed between the cubic and rhombohedral phases at the nanoscale, providing numerous active sites and defect-driven reactivity. The *post-mortem* characterization of the nanorod sensor was conducted using transmission electron microscopy (TEM) and high-resolution transmission electron microscopy (HRTEM) to assess the long-term stability of the material.

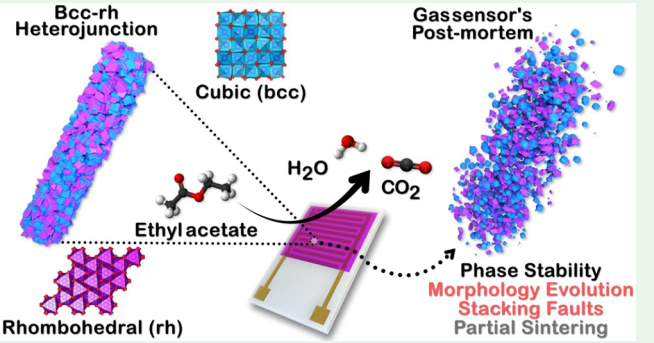

KEYWORDS: *gas sensor, post-mortem, indium oxide, ethyl acetate, cubic-rhombohedral, nanorods*

1. INTRODUCTION

Microorganisms generate microbial volatile organic compounds (MVOCs) through metabolic processes, including the synthesis of DNA and glucose oxidation. Consequently, specific fungal and bacterial species release MVOCs with diverse functional groups, such as aromatic compounds, alcohols, esters, ketones, and others, which are characteristic of these organisms.[1−4] Ethyl acetate is an MVOC that can be produced by the bacterium *Escherichia coli* and is primarily formed during fermentation processes in beer and bread by the fungus *Saccharomyces cerevisiae*.[5−7] Therefore, ethyl acetate is a crucial biomarker for food control, particularly in fruit preservation.[8,9] Consequently, selective and highly responsive ethyl acetate detection ensures food quality and human health safety. These challenges can be addressed by developing a material capable of detecting ethyl acetate in various environments.

Metal oxide semiconductors (MOS) are promising materials for MVOC detection due to their low engineering cost, adjustable structures, and remarkable chemical stability.[10,11] Indium oxide (In_2O_3), an *n*-type semiconductor metal oxide, combines a wide band gap with excellent electrical conductivity, enabling diverse applications when structured at the nanoscale. It is a material with excellent optical and thermal properties, widely employed in solar cells and liquid crystal apparatuses.[12−15] Due to its strong interaction with gaseous molecules, In_2O_3 demonstrates a high potential for gas sensing.[16] The stable crystal phase of In_2O_3 is the cubic bixbyite-type (bcc-In_2O_3, E_g: 2.93 ± 0.15 eV), while the metastable phase is the rhombohedral corundum-type (rh-In_2O_3, E_g: 3.02 ± 0.15 eV).[17,18] These phases can be synthesized by controlling the precursor type during the solvothermal processes, such as cubic-$In(OH)_3$ and ortho-rhombic-InOOH, to obtain bcc-In_2O_3 and rh-In_2O_3 structures, respectively.[18−20] Additionally, the calcination step is crucial for the phase control of In_2O_3.[21] Numerous studies have

Received: March 11, 2025
Revised: May 2, 2025
Accepted: May 5, 2025
Published: May 8, 2025

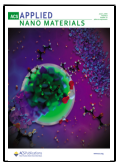

https://doi.org/10.1021/acsanm.5c01487
ACS Appl. Nano Mater. 2025, 8, 11458−11469

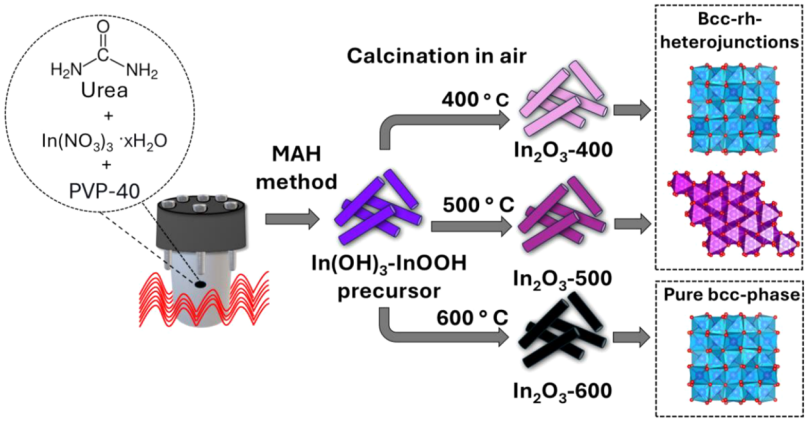

Figure 1. Schematic of the microwave-assisted hydrothermal (MAH) synthesis procedure is followed by calcination of the indium precursor, resulting in mixed-indium oxides (bcc-rh) and in the pure bcc phase.

utilized pure bcc-In_2O_3 and a few with rh-In_2O_3 as gas sensors.[22−27] However, these materials encountered limitations in their sensing performance, including poor selectivity and high response and recovery times.

Enhancements in the gas-sensing properties of In_2O_3 can be achieved through various methods, including the synthesis of In_2O_3-based heterostructures[28] and the deposition of noble metals (Ag, Pt, and Au).[29−31] For instance, He et al. fabricated a Co_3O_4/In_2O_3 *p-n* heterostructure through coprecipitation and pyrolysis, demonstrating a response value 93 times higher to triethylamine compared to the pure In_2O_3 structure.[32] Cao et al. produced cubic-rhombohedral-In_2O_3 (bcc-rh-In_2O_3) microspheres via the hydrothermal procedure, exhibiting a response of 16.9 to acetone and demonstrating excellent selectivity against other gases.[33] For instance, Zhang et al. synthesized Ag nanoparticle-decorated In_2O_3 nanocubes using a one-pot hydrothermal method, exhibiting enhanced sensitivity for 2-butanone, a lower detection limit, and lower response/recovery times than the pure In_2O_3.[34] However, the literature barely reports the application of bcc-rh-In_2O_3 nanorods synthesized through a microwave-assisted hydrothermal method for MVOC monitoring.

As previously mentioned, the development of bcc-In_2O_3 and rh-In_2O_3 structures is associated with the $In(OH)_3$ and InOOH precursors.[18] Furthermore, calcination is crucial when forming bcc-In_2O_3 and rh-In_2O_3 materials at a nanoscale. At elevated calcination temperatures, transitions may occur within the crystalline system due to changes in the oxygen packing and the positioning of indium atoms at higher energy levels.[21] Most reported studies focus on the bcc-In_2O_3 structure due to its crystal phase stability. However, the metastable rh-In_2O_3 offers abundant chemical defects and numerous adsorption sites, which are beneficial for gas-sensing applications.[35,36] In this context, a mixed-phase material combining these crystalline phases based on bcc-rh-In_2O_3 is crucial for enhancing the gas-sensing properties of In_2O_3 through the MOS heterojunction effect.

Stacking faults, a common type of crystallographic defect, profoundly impact the properties of semiconducting oxides by altering carrier mobility and surface reactivity.[37,38] In gas-sensing materials, these defects can modify the adsorption of target gases or oxygen species, affecting sensor sensitivity and stability.[39] The role of stacking faults in bcc-rh-In_2O_3 nanorods, particularly their formation during prolonged sensing operations, can be revealed through meticulous *post-mortem* TEM analysis. In this work, we synthesized a mixed-phase In_2O_3 nanorod composite (combining stable and metastable phases) to enhance MVOC sensing performance compared to a pure bcc-In_2O_3 structure.

2. MATERIALS AND METHODS

2.1. Chemicals and Materials. The reagents were obtained with a high degree of purity from Sigma-Aldrich, including indium(III) nitrate hydrate ($In(NO_3)_3{\cdot}xH_2O$, CAS number 207398-97-8), urea (CH_4N_2O, CAS number 57-13-6), and polyvinylpyrrolidone (PVP-40, CAS number 9003-39-8). The Milli-Q setup (Millipore, 18.2 $M\Omega^{-1}$ at 25 °C) was utilized to purify the deionized (DI) water. The preparation of MVOCs was conducted using high-purity reagents (ethanol, ≥99.5%; benzene, 99.8%; toluene, 99.8%; m-xylene, ≥99%; ethyl acetate, 99.8%; 2-nonanone, ≥99%; and acetone, ≥99.5%).

2.2. Synthesis of In_2O_3 Nanorods. The In_2O_3 nanorods were synthesized based on an adaptation of the reported work by Qin et al.,[22] using a microwave-assisted hydrothermal (MAH) method in two steps. First, 1.2 g of $In(NO_3)_3{\cdot}xH_2O$ and 0.72 g of urea were solubilized in 60 mL of DI water with vigorous agitation for 30 min. After this solubilization, 0.8 g of PVP-40 was included in the solution and stirred until a homogeneous product was obtained. Subsequently, the solution was placed in a polytetrafluoroethylene (PTFE) autoclave, heated for 2 h at 140 °C using a microwave system (2.45 GHz/800 W),[40] and cooled naturally to room temperature. The resulting solution was centrifuged, washed with DI water and ethanol, and dried at 60 °C overnight. Finally, the In_2O_3 structures (In_2O_3-400, In_2O_3-500, and In_2O_3-600) were formed by calcining the $In(OH)_3$-InOOH precipitate at 400, 500, and 600 °C, respectively, with a heating rate of 2 °C min^{-1} for 3 h. The synthesis representation is shown in Figure 1.

2.3. Material Characterizations. The crystal structure of the materials was investigated using an X-ray diffraction (XRD) model Rigaku MiniFlex 300, with a Cu Kα λ = 1.5418 Å, operating at 10 mA and 30 kV. The thermogravimetric analysis (TGA) was carried out by a Shimadzu thermobalance (DTG-60H instrument) in an air atmosphere ranging from 30 to 800 °C (10 °C min^{-1}). Fourier transform infrared spectroscopy (FTIR) was conducted using a PerkinElmer Spectrum Two spectrophotometer, measured in the 400−4000 cm^{-1} region. The surface area measurements were performed via the Brunauer−Emmett−Teller (BET) method with a Micromeritics Gemini VII (2390t). Images of the samples were acquired by Field-emission scanning electron microscopy (FESEM) using a FEI Helios NanoLab 600i (30 kV). Transmission electron microscopy (TEM), high-resolution transmission electron microscopy (HRTEM), and selected area electron diffraction (SAED) analyses were performed with an FEI TECNAI G2F20 microscope. X-ray photoelectron spectroscopy was conducted with a K-alpha (Thermo Scientific) and operated at Kα = 1486 eV. The UV−vis results were

https://doi.org/10.1021/acsanm.5c01487
ACS Appl. Nano Mater. 2025, 8, 11458−11469

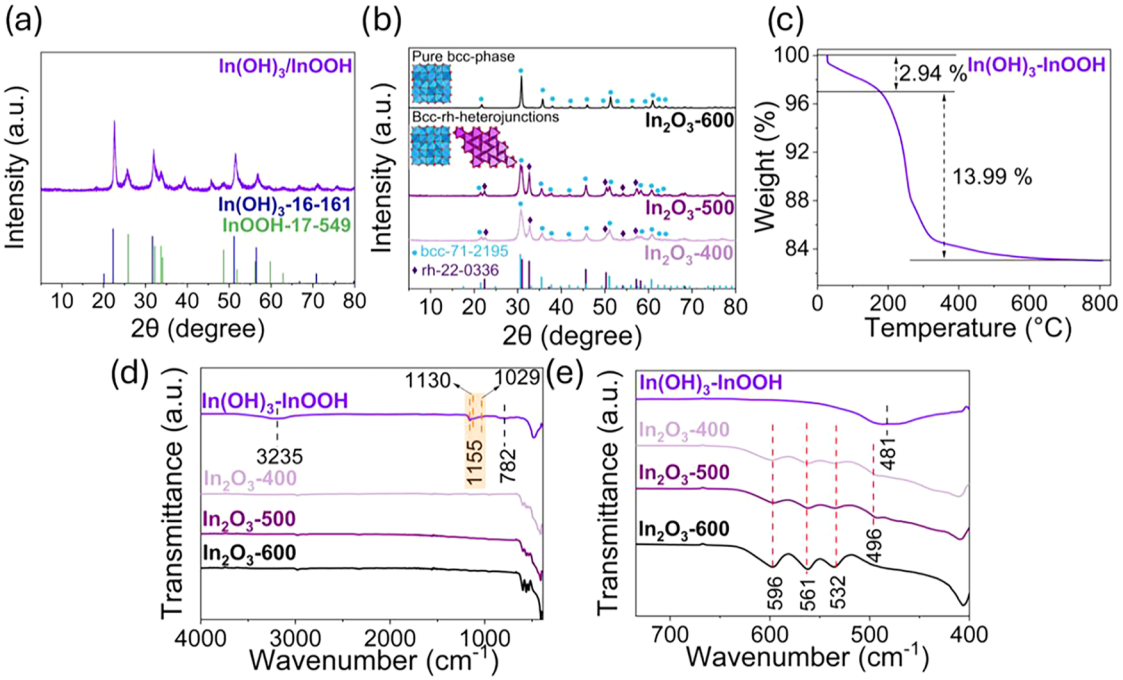

Figure 2. XRD patterns of the (a) $In(OH)_3$-InOOH precursor, (b) In_2O_3-400, In_2O_3-500, and In_2O_3-600. (c) TGA analysis of $In(OH)_3$-InOOH precursor in air. FTIR spectra of $In(OH)_3$/InOOH, In_2O_3-400, In_2O_3-500, and In_2O_3-600 at (d) full wavenumber range and (e) from 700 to 400 cm^{-1}.

obtained using a Varian Cary 5000 spectrophotometer in the diffuse reflectance mode.

2.4. Sensor Measurements and MVOCs Preparation. The In_2O_3 sensors were prepared using 3.00 mg of the sample in an isopropanol dispersion. This dispersion was ultrasonically bathed for 20 min and deposited onto alumina supports containing gold electrodes. The sensors were subsequently heated at 400 °C for 1 h in a tubular oven to eliminate contaminants from the surfaces of the sensor materials. A voltage of 3 V was applied to the prepared sensor substrates, measuring the electrical resistance (R) using a Keithley Source-Meter 2400. Subsequently, a clean air flow of 250 mL min^{-1} was directed into the tubular oven with an inserted thermocouple, and the sensor was placed in the sample holder. The complete gas-sensing measurement setup is shown in Figure S1. The preparation of MVOCs and the setup for sensor measurements were conducted following the previously reported procedures.[41−43]

MVOCs were detected using individual syringes added to the system chamber. Sensing experiments were performed at different operating temperatures (200−400 °C) in dry and humid atmospheres. The sensing measurements at 41 and 90% of relative humidity (RH) were conducted using saturated solutions at room temperature (25 ± 1 °C) of K_2CO_3 and K_2SO_4, respectively, monitored through a HANNA thermohygrometer model HI 9564. The response of the n-type In_2O_3 sensor to selected MVOCs can be estimated via the R_a/R_{MVOC} ratio (sensor's resistance in air/sensor's resistance after MVOC detection).

3. RESULTS AND DISCUSSION

The crystal structure investigation of the synthesized samples before and after calcination was conducted using X-ray diffraction (XRD), as depicted in Figure 2a,b. The $In(OH)_3$-InOOH precursor exhibited peaks indexed to the $In(OH)_3$ cubic phase (JCPDS No. 16-161, c-$In(OH)_3$) and the InOOH orthorhombic phase (JCPDS No. 17-549, o-InOOH). After calcination, the XRD patterns revealed peaks corresponding to a mixed-phase indexed to cubic In_2O_3 (bcc-In_2O_3, JCPDS No. 71-2195) and rhombohedral In_2O_3 (rh-In_2O_3, JCPDS No. 22-0336) for the In_2O_3-400 and In_2O_3-500 samples. Notably, In_2O_3-500 exhibited higher intensity peaks for the metastable phase than In_2O_3-400. Conversely, In_2O_3-600 exhibited peaks corresponding to pure bcc-In_2O_3 material. These findings demonstrate the influence of annealing temperature on the In_2O_3 phase transformations. The thermal decomposition of $In(OH)_3$-InOOH was verified via thermogravimetric analysis (TGA), as presented in Figure 2c. An initial weight loss of 2.94% was observed within the 30 to 200 °C temperature range, attributed to eliminating adsorbed gases (H_2O, CO_2, and O_2). As the temperature increased, an inflection point appeared, followed by forming a band starting at 300 °C. These factors are directly related to $In(OH)_3$ and InOOH decomposition into In_2O_3, occurring from 290 and 400 °C, respectively.[21] The mass loss from 400 to 600 °C was approximately 3%, indicating that the slower heating rate and the 3 h holding period at the target temperature allowed the removal of residual species or adsorbed molecules, which were still present under the fast-heating conditions used in TGA (10 °C min^{-1}). Moreover, this mass loss may be associated with the decomposition of InOOH. A maximum mass loss of 16.93% of the precursor was observed up to 600 °C, corresponding to the phase transition of the precursor mixture into In_2O_3 and the removal of adsorbed gases.

Fourier transform infrared (FTIR) spectroscopy was conducted to obtain the spectra of $In(OH)_3$-InOOH, In_2O_3-400, In_2O_3-500, and In_2O_3-600, as presented in Figure 2d. A band at 3235 cm^{-1} was exhibited for the $In(OH)_3$-InOOH precursor, attributed to the stretching vibration of OH groups from $In(OH)_3$.[44] The precursor also exhibited bands at 1155 cm^{-1} (sharp), 1130 cm^{-1} (shoulder), and 1029 cm^{-1}, attributed to the OH deformations reported by Yang et al.[45] The band centered at 782 cm^{-1} is related to the stretching vibration mode of In−OH.[44] No significant signal corresponding to InOOH was observed, likely due to the low intensity of this phase in the XRD pattern. Figure 2e shows the FTIR

https://doi.org/10.1021/acsanm.5c01487
ACS Appl. Nano Mater. 2025, 8, 11458−11469

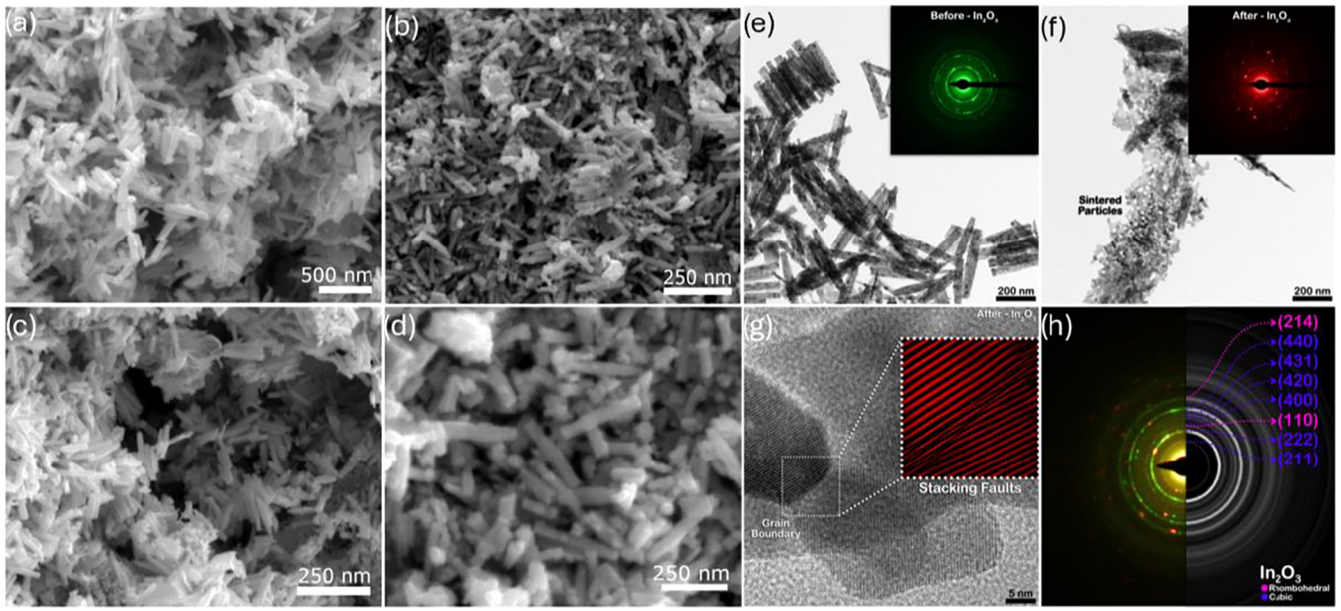

Figure 3. FESEM images of (a) In_2O_3-400, (b) In_2O_3-600, and (c, d) In_2O_3-500. TEM and SAED analyses of (e) In_2O_3-500 and (f) In_2O_3-500 after gas-sensing measurements. (g) HRTEM image of In_2O_3-500 after gas-sensing measurements showing stacking faults. (h) SAED pattern of In_2O_3-500 indexed to the cubic and rhombohedral phases.

spectra of the synthesized samples in the 700−400 cm^{-1} region. The precursor demonstrated a band at 481 cm^{-1}, which is also attributed to the In−OH stretching. The synthesized oxides exhibited three bands at 596, 561, and 532 cm^{-1} correlated to the asymmetric In−O stretching of cubic In_2O_3.[46] The In−O bond vibrations displayed by In_2O_3-400 and In_2O_3-500 and the absence of these vibrations in In_2O_3-600 at 496 cm^{-1} suggest the contribution of the typical rhombohedral metastable phase.

Yu et al.[19] demonstrated the precursor influence of $In(OH)_3$ and InOOH in forming the final In_2O_3 phase. Specifically, stable bcc-In_2O_3 and metastable rh-In_2O_3 are derived from the c-$In(OH)_3$ and o-InOOH precursors, respectively. Furthermore, precursor formation can be controlled through hydrothermal temperature. As illustrated in Reaction 1, it is proposed that In^{3+} species from $In(NO_3)_3{\cdot}xH_2O$ react with OH^- groups from urea to form $In(OH)_3$ during the hydrothermal process. Subsequently, $In(OH)_3$ undergoes annealing to produce the bcc-In_2O_3, as demonstrated in Reaction 2. However, at a higher hydrothermal temperature (140 °C), $In(OH)_3$ experiences dehydration according to Reaction 3, forming InOOH. Finally, rh-In_2O_3 is obtained after calcining the InOOH precursor, as shown in Reaction 4.[33] Additionally, it is suggested that at higher annealing temperatures (600 °C), rh-In_2O_3 is converted to bcc-In_2O_3 due to a transition in the positioning of oxygen and indium atoms, driven by the additional induced energy.[21]

$$In^{3+} + 3OH^- \rightarrow In(OH)_3 \quad (1)$$

$$2In(OH)_3 \rightarrow \text{bcc-}In_2O_3 + 3H_2O \quad (2)$$

$$In(OH)_3 \rightarrow InOOH + H_2O \quad (3)$$

$$2InOOH \rightarrow \text{rh-}In_2O_3 + H_2O \quad (4)$$

FESEM analysis was conducted to investigate the morphological and structural properties of the synthesized samples. Figure 3a,b present the FESEM images of In_2O_3-400 and In_2O_3-600, respectively. As observed, the materials exhibit nanorod structures of In_2O_3, with the In_2O_3-400 sample exhibiting larger nanorods than In_2O_3-600, likely due to the calcination effect. The FESEM images of In_2O_3-500 are shown in Figure 3c,d, illustrating well-defined nanorod structures with an approximate size of 315 nm. Besides the size differences, no significant morphological changes were observed among the synthesized Indium oxides.

Post-mortem characterization of the In_2O_3-500 sensor was conducted using TEM, HRTEM, and SAED techniques after MVOC sensing measurements. Figure 3e presents the TEM image of In_2O_3-500 before MVOC detection, illustrating its porous nanorod structures of In_2O_3. The TEM and HRTEM images of *post-mortem* In_2O_3-500 are shown in Figure 3f,g, respectively. These images reveal significant morphological changes, including partial sintering of nanorods, grain boundary formation, and the appearance of stacking faults. HRTEM analysis revealed stacking faults in the sintered grains, which were not observed in the pristine material. These faults likely form due to thermal and chemical stresses during ethyl acetate sensing at elevated temperatures. Stacking faults can act as scattering sites for charge carriers, potentially impacting electronic transport and contributing to a slight decline in sensor performance after extended operation. Despite these changes, the mixed-phase crystalline structure remained unchanged, as confirmed in Figure 3h, which shows SAED patterns indexed to the cubic and rhombohedral phases of In_2O_3. The identified planes, such as (211) and (440) for the cubic phase and (214) and (110) for the rhombohedral phase, were consistent with the literature. The interplanar spacings measured were 2.93 Å for (211) and 1.81 Å for (440) in the cubic phase, and 2.41 Å for (214) and 3.12 Å for (110) in the rhombohedral phase. These measurements closely corresponded with the XRD data, confirming the coexistence of the two phases.

The nitrogen adsorption and desorption isotherms of In_2O_3-400, In_2O_3-500, and In_2O_3-600 are presented in Figure 4a−c,

https://doi.org/10.1021/acsanm.5c01487
ACS Appl. Nano Mater. 2025, 8, 11458−11469

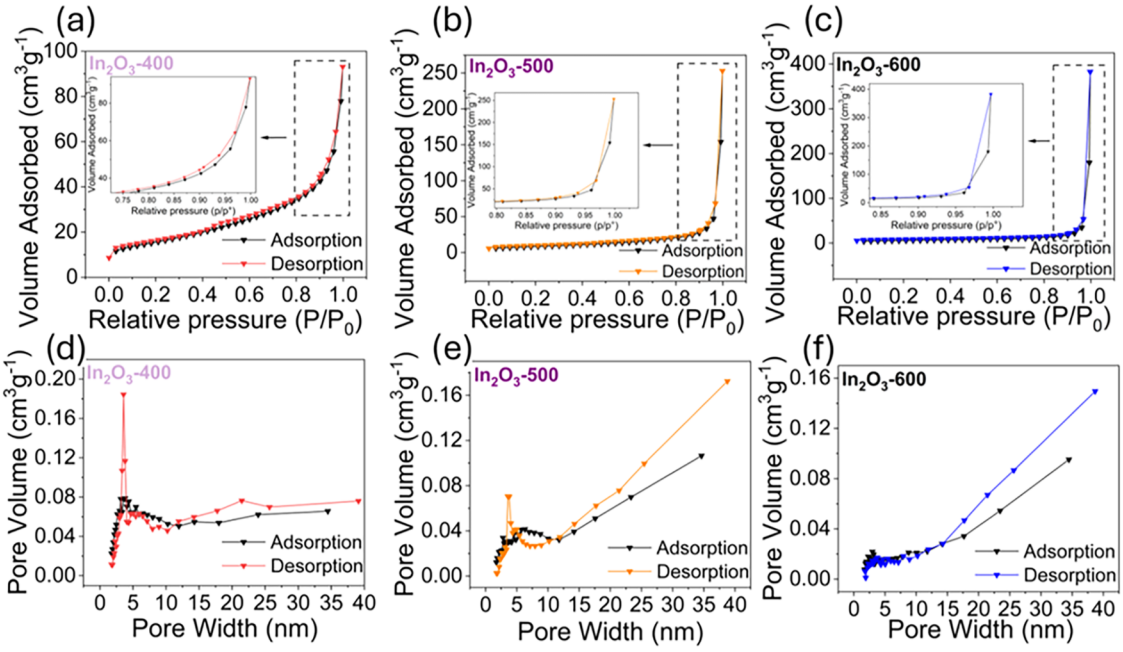

Figure 4. Nitrogen adsorption and desorption isotherms of (a) In_2O_3-400, (b) In_2O_3-500, and (c) In_2O_3-600. Adsorption and desorption pore size distributions of (d) In_2O_3-400, (e) In_2O_3-500, and (f) In_2O_3-600.

respectively. Approximately 0.85−1 of relative pressure (P/P_0) exhibited a similar hysteresis loop demonstrated in the prepared materials, classified as type IV in the IUPAC categorization.[47] This classification is typical for mesoporous solids, further corroborated by the synthesized oxides' adsorption and desorption pore size distributions, as depicted in Figure 4d−f, respectively. The results demonstrate a higher concentration of pore widths within the 3−10 nm range, confirming the mesoporous nature of the synthesized oxides. The synthesized oxides' specific surface area and pore size distribution are also presented in Table 1. The In_2O_3-400 sample exhibited a higher specific surface area of 54.22 $m^2\ g^{-1}$ compared to In_2O_3-500 and In_2O_3-600, which showed 29.36 and 19.40 $m^2\ g^{-1}$ values, respectively. This fact can be clarified by the difference in the calcination temperature, which reduces surface area due to increased crystallite size at higher calcination temperatures. However, the In_2O_3-500 material displayed a higher pore volume of 0.208 $cm^3\ g^{-1}$ and a larger pore size of 4.84 nm compared to the other synthesized samples. These properties enhance the diffusion of MVOC molecules at the surface, improving the sensing properties of In_2O_3-500 and the contribution of the heterojunction effect.

Table 1. Synthesized Materials' BET Surface Area, Pore Volume, and Pore Width

material	surface area ($m^2\ g^{-1}$)	pore volume ($cm^3\ g^{-1}$)[a]	pore width (nm)[b]
In_2O_3-400	54.22	0.119	4.56
In_2O_3-500	29.36	0.208	4.84
In_2O_3-600	19.40	0.054	4.75

[a]Single point adsorption total pore volume of pores less than 1952.438 Å width at P/P° = 0.9900000. [b]BJH Adsorption average pore width (4 V/A by BET).

The XPS survey spectra of In_2O_3-400, In_2O_3-500, and In_2O_3-600 are exhibited in Figure 5a, revealing the elemental composition of the materials' surfaces, which comprises In, O, and C. The presence of C is attributed to atmospheric adsorption of CO_2. No other peaks were observed in the spectra. The high-resolution XPS of the synthesized samples was measured in triplicate to determine the average subpeak quantifications. Figure 5b−d depict the In 3*d* spectra of In_2O_3-400, In_2O_3-500, and In_2O_3-600, respectively. Two peaks can be observed at approximately 451.6−451.5 eV ($3d_{3/2}$) and 444.1−444.0 eV ($3d_{5/2}$). The interval between these peaks is 7.5 eV, related to the spin−orbit of In^{3+} species on the surface of In_2O_3 samples.[48] The O 1s high-resolution results of the samples are

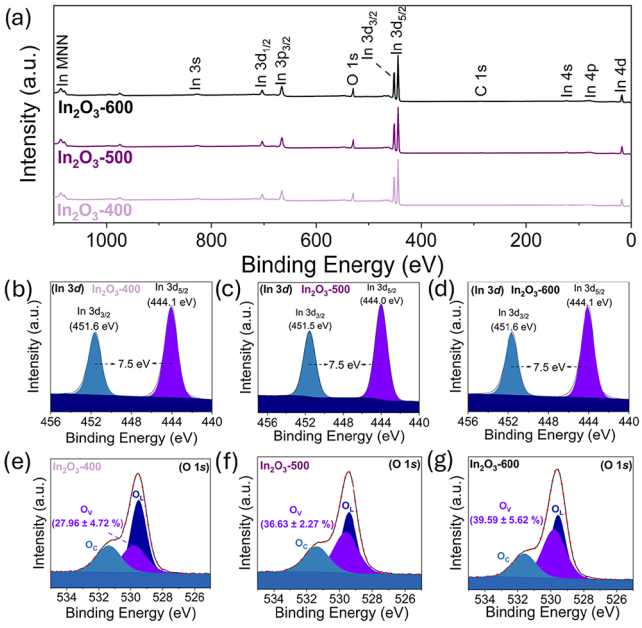

Figure 5. (a) XPS survey spectra of In_2O_3-400, In_2O_3- 500, and In_2O_3-600. XPS high-resolution spectra of In 3*d* of (b) In_2O_3-400, (c) In_2O_3-500, and (d) In_2O_3-600. O 1*s* high-resolution spectra of (e) In_2O_3-400, (f) In_2O_3-500, and (g) In_2O_3-600.

https://doi.org/10.1021/acsanm.5c01487
ACS Appl. Nano Mater. 2025, 8, 11458−11469

demonstrated in Figure 5e–g, presenting the three oxygen components at energies in a range of 529.4–529.5 eV (lattice oxygen, O_L), 529.6–530.1 eV (oxygen vacancy, O_V), and 531.4–531.6 eV (chemisorbed oxygen, O_C).[49,50] As can be seen, the increase in calcination temperature suggests a higher O_V content, as observed in the In_2O_3-600 sample (O_V = 39.59 ± 5.62%) compared to In_2O_3-400 (O_V = 27.96 ± 4.73%) and In_2O_3-500 (36.63 ± 2.27%). A higher concentration of these oxygen defects results in higher electron density and lower material resistance.[51] Table S1 exhibits the relative concentration of the other oxygen species on the materials' surfaces, such as O_L and O_C for In_2O_3-400, In_2O_3-500, and In_2O_3-600. These observed changes in the relative intensities are likely associated with modifications in the crystalline structure, suggesting that the calcination temperature influenced the defect chemistry and surface reactivity of the synthesized samples, which are key factors in the sensing performance.

Figure 6a displays the diffuse reflectance UV–vis spectra of the synthesized samples. The synthesized samples exhibit

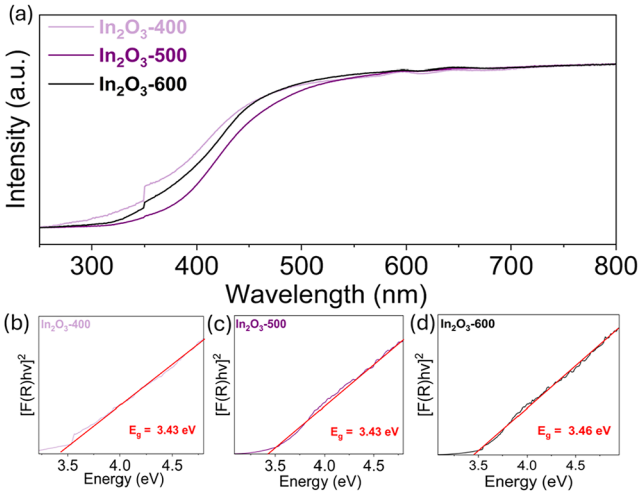

Figure 6. (a) UV–vis diffuse reflectance results of In_2O_3-400, In_2O_3-500, and In_2O_3-600. Band-gap (E_g) values using Tauc's plot of (b) In_2O_3-400, (c) In_2O_3-500, and (d) In_2O_3-600.

similar reflectance bands ranging from 500 to 350 nm, with slight variations in their intensities. The obtained spectra align with the previously reported literature data.[52,53] These optical properties analyses suggest a heterojunction effect in the radiation reflectance process of the In_2O_3-400 and In_2O_3-500 samples. The band-gap (E_g) values of the oxides were determined using eqs 5 and 6, based on the semiconductor correlation:[54,55]

$$(ahv)^2 = K(hv - E_g) \tag{5}$$

$$a = (1 - D)^2/2D \tag{6}$$

Equation 5 represents the correlation for the E_g calculation, where a is the absorption coefficient, K is the proportionally constant, and hv is the photon energy. The Kubelka–Munk equation (eq 6) was used to determine the value of a, where D is the experimentally measured diffuse reflectance. The determined E_g values of the synthesized In_2O_3-400, In_2O_3-500, and In_2O_3-600 are shown in Figure 6b–d, respectively. The In_2O_3-400 and In_2O_3-500 heterostructures exhibited an E_g of 3.43 eV, which increased to 3.46 eV for the pure In_2O_3-600. The lower values can be attributed to the heterojunction effect, which reduces the E_g due to the Fermi equilibrium process and electron redistribution. These estimated values are consistent with previous works.[56,57]

The MVOC measurements were conducted within an operating temperature range of 200 to 400 °C, with no significant results observed below 200 °C. The measurements of the synthesized materials for 100 ppm of MVOCs at operating temperatures of 300 °C for In_2O_3-400 and 350 °C for In_2O_3-500 and In_2O_3-600 are presented in Figure 7a. The samples exhibited the highest response to ethyl acetate, with the In_2O_3-400 and In_2O_3-500 heterostructures showing responses more than seven times higher than pure In_2O_3-600, suggesting the contribution of the metastable phase in the sensing process. Furthermore, In_2O_3-500 demonstrated the highest response value of 548 for ethyl acetate at the optimum temperature compared to the In_2O_3-400 and In_2O_3-600, which showed responses of 352 and 47, respectively. The selectivity index (SI) is measured based on the sensor's ability to distinguish the target gas from potential interfering gases. The In_2O_3-500 sensor exhibited the highest SI value of 3.8 at 250 °C, calculated as the ratio of the response to ethyl acetate over ethanol. At the optimal working temperature of 350 °C, the SI reached 2.1, surpassing the values obtained for other samples, as shown in Figure 7b. The SI for other interfering MVOCs is presented in Figure S2, with the In_2O_3-500 sensor exhibiting higher SI values of 17.8 for 2-nonanone (S2) and 4.73 for acetone (S3) at 350 °C, respectively. These results highlight the good selectivity of the mixed-phase In_2O_3-500 material, suggesting a heterojunction effect on ethyl acetate detection. Figure 7c summarizes the responses of the samples to ethyl acetate detection at different temperatures. As depicted, the highest responses to 100 ppm of ethyl acetate were observed at 300 and 350 °C, where O^- ions are the dominant oxygen species in the atmosphere, typical for *n*-type sensing mechanisms.[58] The In_2O_3-500 responses to 100 ppm of various MVOCs concerning temperature are summarized in Figure S3, exhibiting the most favorable operation temperature of 350 °C for most tested MVOCs. The response/recovery times for 100 ppm of ethyl acetate for In_2O_3-400, In_2O_3-500, and In_2O_3-600 at their respective optimal working temperatures (300 and 350 °C) in dry atmosphere are shown in Figure 7d–f. The In_2O_3-500 sensor exhibited a faster response time of 1.8 s compared to the other materials, with 3.5 and 5.0 s for In_2O_3-400 and In_2O_3-600, respectively. However, the recovery times were 1463.7, 1748.2, and 961.6 s for In_2O_3-400, In_2O_3-500, and In_2O_3-600, respectively. A possible explanation for the prolonged recovery time (1748.2 s) of In_2O_3-500 is the strong interaction between the chemisorbed oxygen sites and the ethyl acetate molecules, which results in a high response, hinders the desorption process and delays the sensor's reversibility.

The In_2O_3-500 responses to different concentrations (ppm) of ethyl acetate at 350 °C are shown in Figure 7g. The sensor demonstrated excellent performance across a wide concentration range (2–500 ppm), which is crucial for detecting this MVOC in various contexts, such as disease diagnosis and monitoring exposure in industrial environments. These results are further supported by Figure 7h, which shows dynamic responses ranging from 7.4 to 1340 as a function of ethyl acetate concentration (2–500 ppm). As illustrated in Figure 7i, a linear equation was obtained through linear regression of the experimental data points at low concentrations to estimate the

https://doi.org/10.1021/acsanm.5c01487
ACS Appl. Nano Mater. 2025, 8, 11458–11469

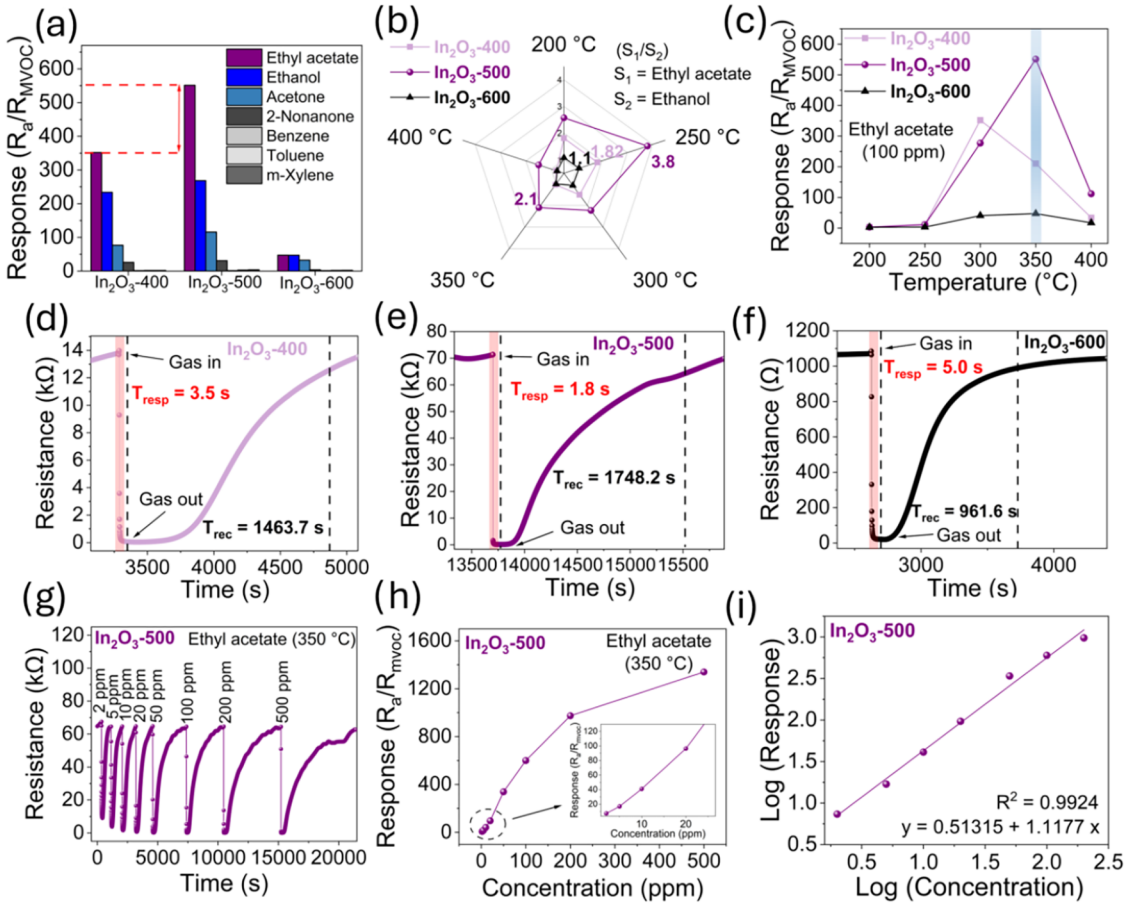

Figure 7. (a) Sensor measurements to 100 ppm for different MVOCs of In_2O_3-400, In_2O_3-500, and In_2O_3-600 at their optimum temperatures. (b) Radar graph of selectivity index to ethyl acetate in different operation temperatures. (c) Ethyl acetate responses as a function of temperature. Response and recovery times in a dry atmosphere to 100 ppm of ethyl acetate for (d) In_2O_3-400, (e) In_2O_3-500, and (f) In_2O_3-600 at their respective optimum temperatures. In_2O_3-500 ethyl acetate sensing results in a dry atmosphere at 350 °C to (g) different concentrations, (h) curve response versus concentration, and (i) linear fit of logarithm response versus logarithm concentration.

theoretical detection limit of In_2O_3-500 for ethyl acetate. By extrapolating a response value of 1.1, the detection limit was determined to be approximately 525 ppb, confirming the detection capability of the In_2O_3-500 heterostructure for ethyl acetate detection. This great sensing performance can be linked to the bcc-rh heterostructure outcome.

The long-term stability of the In_2O_3-500 sensor for ethyl acetate detection was evaluated, as exhibited in Figure 8a. Measurements were conducted over 8 days at a temperature of 350 °C. The figure shows that the sensor exhibited high sensitivity, with an average response of 551.4 ± 39.5 to 100 ppm of ethyl acetate. Notably, a slight decline in response was observed after 5 days, likely due to the elevated operating temperature and the extensive number of measurements conducted, which negatively affected the sensing performance. This phenomenon is hypothesized to lead to stacking faults forming in the grain boundaries of In_2O_3, as discussed in the TEM and HRTEM analyses. Stacking faults, which disrupt the regular stacking sequence of crystal planes, can influence the sensing mechanism by modifying the electronic properties of the material. For instance, they create localized states that may enhance the adsorption of oxygen species or disrupt the uniform flow of charge carriers, thereby affecting sensing performance.

Additionally, 20 application cycles to 10 ppm of ethyl acetate at 350 °C were performed to assess the reversibility of In_2O_3-500 (Figure 8b). The average response during these cycles was 7.8 ± 0.3, demonstrating excellent reversibility and stability. These findings were crucial for understanding the long-term stability of the In_2O_3-500 sensor.

The humidity effect on the sensing effectiveness of In_2O_3-500 was investigated at 350 °C and achieved by exposing the sensor to 100 ppm of various MVOCs at RH levels of 41 and 90%, as depicted in Figure 9. A significant reduction in the sensing performance was observed for all tested MVOCs. Notably, In_2O_3-500 still strongly responded to ethyl acetate even at 90% RH (response 79.78, vs 160.65 at 41% RH). The reduced response under humidity is attributed to chemisorbed O^- reacting with H_2O to form OH^- groups at active sites. These hydroxyls increase the baseline conductance (lower the sensor's resistance), effectively diminishing the sensor's response magnitude.[59,60] Figure S4 shows the difference in the R_a values and response/recovery times to ethyl acetate detection in dry and humid atmospheres of In_2O_3-500. As previously discussed, the presence of water decreases the sensor's resistance, as observed at 41 and 90% RH, with R_a values of 28.3 and 18.9 kΩ, respectively, compared to 71.4 kΩ in a dry atmosphere. However, the response times under humid conditions remained similar as in dry measurements, with a slight difference in the recovery times due to the decreased responses.

https://doi.org/10.1021/acsanm.5c01487
ACS Appl. Nano Mater. 2025, 8, 11458−11469

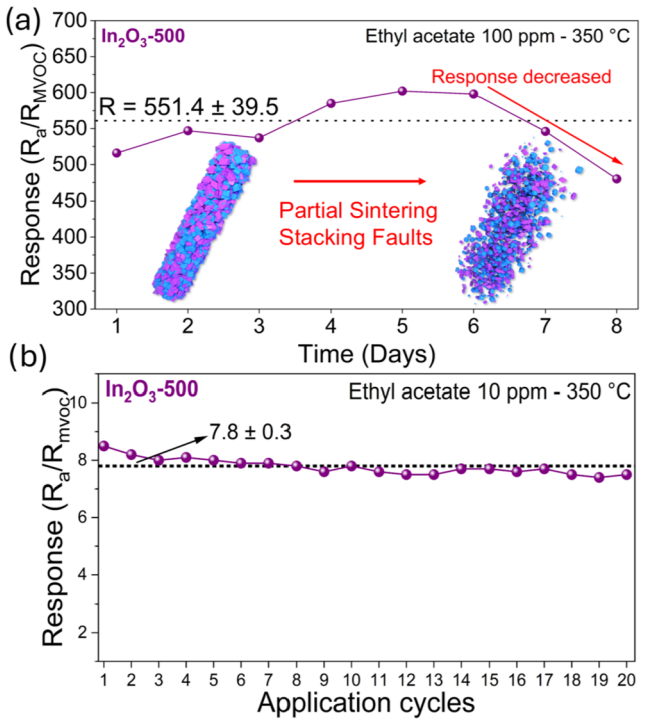

Figure 8. In_2O_3-500 repeatability responses (a) within 8 days for detecting 100 ppm of ethyl acetate and (b) 20 application cycles to 10 ppm of ethyl acetate at 350 °C and dry air.

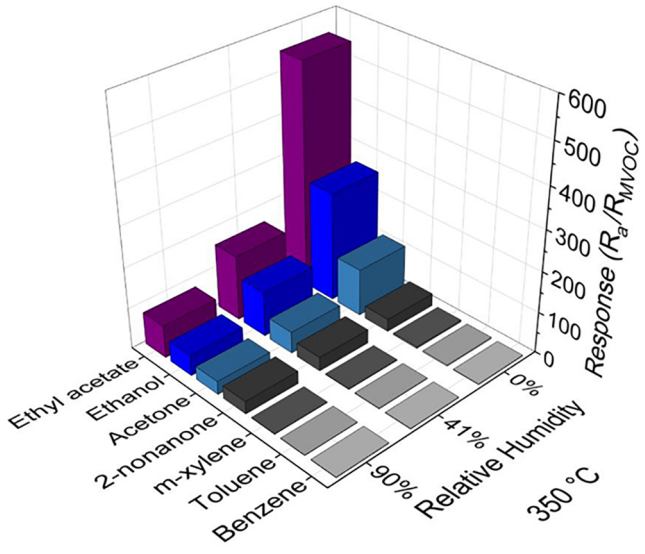

Figure 9. Responses of the In_2O_3-500 sensor at 350 °C to 100 ppm for the selected MVOCs in different *RH* atmospheres measured at 25 ± 1 °C.

When air exposure, the gas-sensing mechanism for *n*-type semiconductors is correlated with the oxygen molecules (O_2) adsorption on the material's surface. The most abundant oxygen species in the atmosphere at 350 °C is O^-.[58] In this way, the pure bcc nanorod (In_2O_3-600) demonstrates chemisorbed O^- ions, which capture free electrons from the conduction band during the process of oxygen molecule adsorption. This process leads to the formation of a depletion layer on the sensor's surface, increasing the resistance. It is suggested that when In_2O_3-600 is exposed to a reduction gas, such as ethyl acetate, the O^- active sites react with the target MVOC, producing CO_2 and H_2O, as exhibited in Figure 10a. The confined electrons are then released back into the conduction band, decreasing the resistance, as shown in eqs 7 and 8:[61]

$$C_4H_8O_{2(gas)} \leftrightarrow C_4H_8O_{2(ads)} \quad (7)$$

$$C_4H_8O_{2(ads)} + 10O^-_{(ads)} \rightarrow 4CO_{2(gas)} + 4H_2O_{(gas)} + 10e^- \quad (8)$$

Due to the heterojunction effect, the In_2O_3-400 and In_2O_3-500 sensors exhibited enhanced sensing performance for ethyl acetate. Electrons flow from the higher to the lower Fermi level until equilibrium is reached. In other words, electrons transfer from the rh to the bcc phase when both are in contact, as shown in Figure 10b. This process increases electron density and the number of active sites for adsorbed oxygen at the bcc interface, establishing an accumulation layer. Conversely, electron loss forms a depletion layer at the rhombohedral interface.[18,33] Thus, when the In_2O_3-400 or In_2O_3-500 heterostructures nanorods are exposed to ethyl acetate, more active sites based on O^- species react with the target MVOC, increasing the sensitivity (Figure 10c). In_2O_3-500 exhibited a more significant contribution of the metastable phase, higher porous volume, and increased surface O_V content compared to In_2O_3-400, suggesting a possible explanation for the superior sensing performance relative to the other synthesized heterostructure.

The In_2O_3-500 sensor demonstrated a higher pore volume of 0.208 $cm^3\ g^{-1}$ and a larger pore width of 4.84 nm compared to the other synthesized samples, as revealed by the BET findings. Consequently, it is suggested that the adsorption of gas molecules was enhanced. Thus, it is essential to discuss the effects of calcination temperature. The In_2O_3-400 material exhibited a higher BET surface area than In_2O_3-500 and In_2O_3-600, which may be associated with the crystallite size effect. However, the In_2O_3-500 nanorods showed the best ethyl acetate detection performance, likely due to the heterojunction effect.

Furthermore, all samples exhibited similar nanorod morphologies. While In_2O_3-400 had the highest surface area, its lower contribution of the rhombohedral phase (and thus fewer heterojunctions) likely limited its performance. In contrast, In_2O_3-500, with a slightly lower surface area but more heterojunction interfaces and oxygen vacancies, achieved the best balance for ethyl acetate detection.

Table 2 compares the sensing properties of ethyl acetate detection in this work with those found in the literature. Our sensor demonstrated a higher sensitivity to ethyl acetate in dry and humid conditions than all comparisons. Although the optimum working temperature and recovery time were higher, the sensor showed excellent response time in different atmospheres. Therefore, the In_2O_3-500 heterostructure achieved promising results for ethyl acetate detection.

4. CONCLUSIONS

A mixed-phase material based on a heterojunction of stable and metastable crystalline phases of bcc-rh-In_2O_3 nanorods was synthesized through the MAH method to detect MVOC. The calcination temperature was crucial in achieving pure bcc-In_2O_3 and heterostructures of bcc-rh-In_2O_3 nanorods, with temperatures set at 600, 500, and 400 °C, respectively. The In_2O_3-500 sensor exhibited superior sensing properties for ethyl acetate detection compared to the other synthesized

https://doi.org/10.1021/acsanm.5c01487
ACS Appl. Nano Mater. 2025, 8, 11458−11469

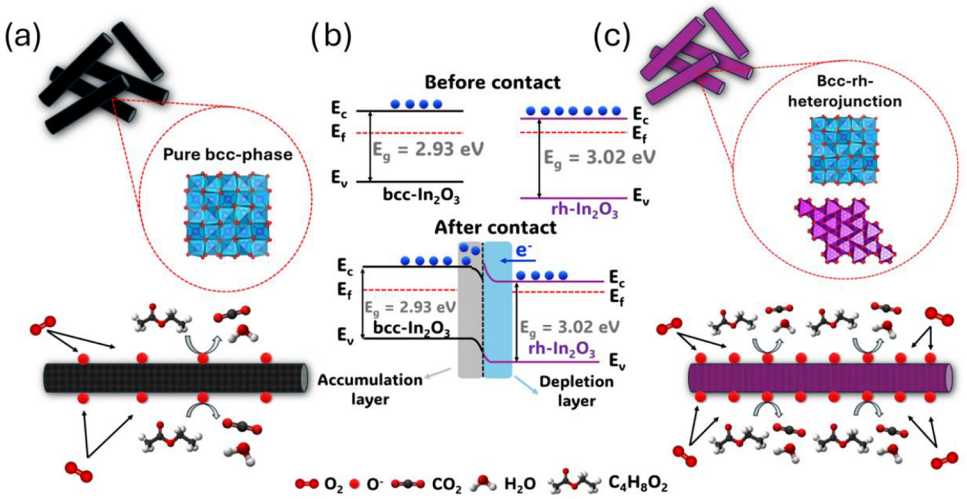

Figure 10. (a) Detection mechanism of ethyl acetate for pure bcc-In_2O_3 (In_2O_3-600). (b) Schematic representation of the heterojunction formation between bcc-In_2O_3 and rh-In_2O_3 phases. (c) Detection mechanism of ethyl acetate for the bcc-rh-In_2O_3 heterostructure (In_2O_3-400 or In_2O_3-500).

Table 2. Comparison of Ethyl Acetate Sensing Properties among Different Reported Sensors

material	temp. (°C)	RH (%)	conc. (ppm)	response (R_g/R_a or R_a/R_g)	response time (s)	recovery time (s)	refs
Al-doped In_2O_3	184	30	100	56.3			61
$NiFe_2O_4$	120		200	64.27	32	31	62
Au decorated ZnO	240		100	102	10	13	63
$CoWO_4/\alpha$-Fe_2O_3	206		100	21.04	7	9	64
$PrFeO_3/\alpha$-Fe_2O_3	206	dry	100	22.85	8	9	65
In_2O_3-500	350	dry	100	548	1.8	1748.2	this work
	350	41	100	160.65	2	945.9	this work
	350	90	100	79.78	1.5	647.1	this work

samples. The In_2O_3-500 nanorods demonstrated a higher response of 548 to 100 ppm of ethyl acetate at 350 °C and dry air. Furthermore, In_2O_3-500 exhibited remarkable selectivity, a low theoretical detection limit, fast response time, remarkable performance under humid conditions, and reasonable stability.

Our research presented a nanoscale material exhibiting excellent properties as an MVOC sensor. Post-mortem HRTEM revealed the formation of stacking faults and grain growth after prolonged operation, indicating some performance degradation mechanisms. Such analyses of long-term structural changes are rarely reported in gas sensors and provide valuable insights into sensor durability. In this context, the In_2O_3-500 nanorods demonstrated high sensitivity and selectivity for ethyl acetate, making it a promising sensor for food quality control and human health monitoring applications. These applications can reduce unnecessary food waste, simplify disease diagnosis, and enhance industrial environmental monitoring. MVOC sensors are rarely reported, particularly those employing mixed-phase bcc-rh-In2O3 nanorods. However, this sensor requires a high operation temperature (350 °C), which poses challenges for practical applications. Strategies such as noble metal deposition could be implemented in future studies to address this, reducing the operating temperature and enabling its use in real and complex samples. Combined with the mixed-phase approach demonstrated here, this strategy could pave the way for practical MVOC sensors for food safety applications.

■ ASSOCIATED CONTENT

Supporting Information

The Supporting Information is available free of charge at https://pubs.acs.org/doi/10.1021/acsanm.5c01487.

Analyses of O 1s XPS high-resolution quantification of the synthesized samples; gas-sensing measurement setup; graphic with selectivity index of ethyl acetate between the main interfering MVOCs; responses to 100 ppm of different MVOCs in dry air as a function of temperature for In_2O_3-500; and R_a values of In_2O_3-500 in different RH conditions: (a) dry atmosphere, (b) 41%, and (c) 90% for ethyl acetate detection at 350 °C (PDF)

■ AUTHOR INFORMATION

Corresponding Author

Diogo Paschoalini Volanti − *Laboratory of Materials for Sustainability (LabMatSus), São Paulo State University (UNESP), 15054-000 São José do Rio Preto, SP,, Brazil;* orcid.org/0000-0001-9315-9392; Email: diogo.volanti@unesp.br

Authors

Gustavo Sanghikian Marques dos Santos − *Laboratory of Materials for Sustainability (LabMatSus), São Paulo State University (UNESP), 15054-000 São José do Rio Preto, SP,, Brazil;* orcid.org/0000-0002-4894-5914

Reinaldo dos Santos Theodoro − *Laboratory of Materials for Sustainability (LabMatSus), São Paulo State University*

https://doi.org/10.1021/acsanm.5c01487
ACS Appl. Nano Mater. 2025, 8, 11458−11469

(UNESP), 15054-000 São José do Rio Preto, SP,, Brazil; orcid.org/0000-0002-6069-7167

Gabriela Oliveira Gera − *Federal University of ABC (UFABC), Center for Natural and Human Sciences, 09210580 Santo André, SP,, Brazil*

Tarcísio Micheli Perfecto − *Brazilian Nanotechnology National Laboratory, Brazilian Center for Research in Energy and Materials (CNPEM), 13083-970 Campinas, SP,, Brazil;* orcid.org/0000-0002-5301-7362

Complete contact information is available at: https://pubs.acs.org/10.1021/acsanm.5c01487

Author Contributions

The manuscript was written with contributions from all authors. All authors have approved the final version of the manuscript.

Funding

The Article Processing Charge for the publication of this research was funded by the Coordenacao de Aperfeicoamento de Pessoal de Nivel Superior (CAPES), Brazil (ROR identifier: 00x0ma614).

Notes

The authors declare no competing financial interest.

■ ACKNOWLEDGMENTS

We acknowledge the Coordenação de Aperfeiçoamento de Pessoal de Nível Superior - Brazil (CAPES) (Finance Code 001, and grant number 88887.920954/2023-00), the São Paulo Research Foundation (FAPESP) (grant numbers #2024/03388-4, #2022/05381-1, #2020/06421-1, #2024/12700-1, #2024/15260-2, and #2022/14720-4), and the National Council for Scientific and Technological Development (CNPq) (grant number 311453/2021-0). We thank LSQA/IBILCE/UNESP for providing the XRD and FTIR analyses. FESEM and TEM facilities were supplied by LME-IQ-UNESP and LCE/DEMa/UFSCar, respectively. We acknowledge LabCat DEQ/UFSCar for TGA analysis. The Brazilian Nanotechnology National Laboratory (LNNano) supplied the XPS facility (proposal 20241266).

■ REFERENCES

(1) Korpi, A.; Järnberg, J.; Pasanen, A. L. Microbial Volatile Organic Compounds. *Crit. Rev. Toxicol.* **2009**, *39*, 139−193.

(2) Lemfack, M. C.; Gohlke, B. O.; Toguem, S. M. T.; Preissner, S.; Piechulla, B.; Preissner, R. MVOC 2.0: A Database of Microbial Volatiles. *Nucleic Acids Res.* **2018**, *46* (D1), D1261−D1265.

(3) Montejano-Ramírez, V.; Ávila-Oviedo, J. L.; Campos-Mendoza, F. J.; Valencia-Cantero, E. Microbial Volatile Organic Compounds: Insights into Plant Defense. *Plants* **2024**, *13*, 2013.

(4) Kemmler, E.; Lemfack, M. C.; Goede, A.; Gallo, K.; Toguem, S. M. T.; Ahmed, W.; Millberg, I.; Preissner, S.; Piechulla, B.; Preissner, R. MVOC 4.0: A Database of Microbial Volatiles. *Nucleic Acids Res.* **2025**, *53* (D1), D1692−D1696.

(5) Bohnenkamp, A. C.; Wijffels, R. H.; Kengen, S. W. M.; Weusthuis, R. A. Co-Production of Hydrogen and Ethyl Acetate in *Escherichia Coli*. *Biotechnol Biofuels* **2021**, *14* (1), No. 192.

(6) Verstrepen, K. J.; Van Laere, S. D. M.; Vanderhaegen, B. M. P.; Derdelinckx, G.; Dufour, J. P.; Pretorius, I. S.; Winderickx, J.; Thevelein, J. M.; Delvaux, F. R. Expression Levels of the Yeast Alcohol Acetyltransferase Genes ATF1, Lg-ATF1, and ATF2 Control the Formation of a Broad Range of Volatile Esters. *Appl. Environ. Microbiol.* **2003**, *69* (9), 5228−5237.

(7) Shi, W.; Li, J.; Chen, Y.; Liu, X.; Chen, Y.; Guo, X.; Xiao, D. Metabolic Engineering of *Saccharomyces Cerevisiae* for Ethyl Acetate Biosynthesis. *ACS Synth. Biol.* **2021**, *10* (3), 495−504.

(8) Concina, I.; Falasconi, M.; Gobbi, E.; Bianchi, F.; Musci, M.; Mattarozzi, M.; Pardo, M.; Mangia, A.; Careri, M.; Sberveglieri, G. Early Detection of Microbial Contamination in Processed Tomatoes by Electronic Nose. *Food Control* **2009**, *20* (10), 873−880.

(9) Leng, P.; Hu, H. W.; Cui, A. H.; Tang, H. J.; Liu, Y. G. HS-GC-IMS with PCA to Analyze Volatile Flavor Compounds of Honey Peach Packaged with Different Preservation Methods during Storage. *LWT* **2021**, *149*, No. 111963.

(10) Hussain, S.; Begi, A. N.; Amu-Darko, J. N. O.; Zhang, X.; Qiao, G.; Liu, G.; Hussain, S.; Yusuf, K.; Manavalan, R. K.; Begi, A. N.; Iqbal, A. MOF-Derived Mo-Doped Co_3O_4: A Hierarchical Yeast-like Structure for Superior Carbon Monoxide Sensing. *Sens. Actuators, B* **2024**, *420*, No. 136489.

(11) Hussain, S.; Wang, S.; Amu-Darko, J. N. O.; Begi, A. N.; Yusuf, K.; Ibrahim, T. K.; Iqbal, A.; Manavalan, R. K.; Zhang, X.; Qiao, G. MOF-Derived La-Doped ZnO Dodecahedron Nanostructures for Efficient Detection of NO_2 Gas. *Sens. Actuators, B* **2025**, *425*, No. 136954.

(12) Ko, T. S.; Chu, C. P.; Chen, J. R.; Lu, T. C.; Kuo, H. C.; Wang, S. C. Tunable Light Emissions from Thermally Evaporated In_2O_3 Nanostructures Grown at Different Growth Temperatures. *J. Cryst. Growth* **2008**, *310* (7−9), 2264−2267.

(13) Emziane, M.; Le Ny, R. Opto-Electrical Characterization of γ-$In_2Se_{2.5}Te_{0.5}$thin Layers☆. *Mater. Res. Bull.* **2000**, *35* (11), 1849−1857.

(14) Hamberg, I.; Granqvist, C. G. Evaporated Sn-Doped In_2O_3 Films: Basic Optical Properties and Applications to Energy-Efficient Windows. *J. Appl. Phys.* **1986**, *60* (11), R123−R160.

(15) Granqvist, C. G. Transparent Conductive Electrodes for Electrochromic Devices: A Review. *Appl. Phys. A:Solids Surf.* **1993**, *57* (1), 19−24.

(16) Shi, Y.; Li, X.; Sun, X. F.; Shao, X.; Wang, H. Y. Strategies for Improving the Sensing Performance of In_2O_3-Based Gas Sensors for Ethanol Detection. *J. Alloys Compd.* **2023**, *963*, No. 171190.

(17) Li, P.; Fan, H.; Cai, Y.; Xu, M.; Long, C.; Li, M.; Lei, S.; Zou, X. Phase Transformation (Cubic to Rhombohedral): The Effect on the NO_2 Sensing Performance of Zn-Doped Flower-like In_2O_3 Structures. *RSC Adv.* **2014**, *4* (29), 15161−15170.

(18) Chen, F.; Yang, M.; Wang, X.; Song, Y.; Guo, L.; Xie, N.; Kou, X.; Xu, X.; Sun, Y.; Lu, G. Template-Free Synthesis of Cubic-Rhombohedral-In_2O_3 Flower for Ppb Level Acetone Detection. *Sens. Actuators, B* **2019**, *290*, 459−466.

(19) Yu, D.; Wang, D.; Qian, Y. Synthesis of Metastable Hexagonal In_2O_3 Nanocrystals by a Precursor-Dehydration Route under Ambient Pressure. *J. Solid State Chem.* **2004**, *177* (4−5), 1230−1234.

(20) Chen, C.; Chen, D.; Jiao, X.; Wang, C. Ultrathin Corundum-Type In_2O_3 Nanotubes Derived from Orthorhombic InOOH: Synthesis and Formation Mechanism. *Chem. Commun.* **2006**, No. No. 44, 4632−4634.

(21) Nielsen, I. G.; Sommer, S.; Iversen, B. B. Phase Control for Indium Oxide Nanoparticles. *Nanoscale* **2021**, *13* (7), 4038−4050.

(22) Qin, W.; Yuan, Z.; Gao, H.; Meng, F. Ethanol Sensors Based on Porous In_2O_3 Nanosheet-Assembled Micro-Flowers. *Sensors* **2020**, *20* (12), No. 3353.

(23) Wagner, T.; Sauerwald, T.; Kohl, C. D.; Waitz, T.; Weidmann, C.; Tiemann, M. Gas Sensor Based on Ordered Mesoporous In_2O_3. *Thin Solid Films* **2009**, *517* (22), 6170−6175.

(24) Liu, X.; Jiang, L.; Jiang, X.; Tian, X.; Sun, X.; Wang, Y.; He, W.; Hou, P.; Deng, X.; Xu, X. Synthesis of Ce-Doped In_2O_3 Nanostructure for Gas Sensor Applications. *Appl. Surf. Sci.* **2018**, *428*, 478−484.

(25) Sui, N.; Zhang, P.; Zhou, T.; Zhang, T. Selective Ppb-Level Ozone Gas Sensor Based on Hierarchical Branch-like In_2O_3 Nanostructure. *Sens. Actuators, B* **2021**, *336*, No. 129612.

(26) Nguyen, T. T. D.; Choi, H. N.; Ahemad, M. J.; Van Dao, D.; Lee, I. H.; Yu, Y. T. Hydrothermal Synthesis of In_2O_3 Nanocubes for

Highly Responsive and Selective Ethanol Gas Sensing. *J. Alloys Compd.* **2020**, *820*, No. 153133.
(27) Liang, T. T.; Kim, D. S.; Yoon, J. W.; Yu, Y. T. Rapid Synthesis of Rhombohedral In_2O_3 Nanoparticles via a Microwave-Assisted Hydrothermal Pathway and Their Application for Conductometric Ethanol Sensing. *Sens. Actuators, B* **2021**, *346*, No. 130578.
(28) Yuan, Z. Y.; Yang, F.; Zhu, H. M.; Meng, F. L.; Ibrahim, M. High-Response n-Butanol Gas Sensor Based on ZnO/In_2O_3 Heterostructure. *Rare Metals* **2023**, *42* (1), 198−209.
(29) Li, D.; Li, Y.; Wang, X.; Sun, G.; Cao, J.; Wang, Y. Improved TEA Sensitivity and Selectivity of In_2O_3 Porous Nanospheres by Modification with Ag Nanoparticles. *Nanomaterials* **2022**, *12*, 1532.
(30) Yang, B.; Wang, X.; Wang, Y.; Yi, G.; Zhou, J.; Zhang, Y. Preparation of Pt-Modified In_2O_3 Nanobundles with Enhanced Formaldehyde Gas Sensing Performance. *J. Porous Mater.* **2024**, *31*, 2091−2100.
(31) Liu, H.; Liu, Q.; Feng, Y.; Xu, D.; Tang, P.; Li, D. Facile Assembly of Au Nanoparticles Modified Hierarchical Mesoporous In_2O_3 for Highly Sensitive Ethanol Gas Detection. *Sens. Actuators, B* **2024**, *402*, No. 135103.
(32) He, J.; Cheng, Z.; Liu, Z.; Yin, M.; Zhang, Y.; Han, L.; Xu, Y. Epitaxial Growth of Co_3O_4/In_2O_3 p-n Heterostructure with Rich Oxygen Vacancies for Ultrahigh Triethylamine Sensing. *Sens. Actuators, B* **2024**, *400*, No. 134881.
(33) Cao, E.; Wu, L.; Zhang, Y.; Sun, L.; Yu, Z.; Nie, Z. Hydrothermal Synthesis of Cubic-Rhombohedral-In_2O_3 Microspheres with Superior Acetone Sensing Performance. *Appl. Surf. Sci.* **2023**, *613*, No. 156045.
(34) Zhang, H.; Guo, Y.; Gao, H.; Meng, F. Preparation of 2-Butanone Gas Sensor Based on Ag-Decorated In_2O_3 Nanocube with High Response and Low Detection Level. *Chemosensors* **2023**, *11* (5), 288.
(35) Jin, Z.; Mou, Y.; Zhao, J.; Chen, C.; Zhou, H.; Xiang, N.; Wang, F.; Wang, Z.; Liu, J.; Wu, L. Crystalline Structure Controlled of In_2O_3 Sensing Platforms for Sensitive H_2S Performance at Low Temperature. *Sens. Actuators, B* **2024**, *401*, No. 135026.
(36) Jin, Z.; Mou, Y.; Zhao, J.; Liu, F.; Liu, L.; Zhao, D.; Li, S.; Liu, J.; Wu, L. Anchoring Ni Atomic Clusters on Yolk-Shell In_2O_3 Microspheres for Highly Sensitive, Ultra-Rapid Responding/Recovering Ppb-Level NO_2 Detections. *Chem. Eng. J.* **2024**, *499*, No. 156531.
(37) Wang, Y.; Wang, T.; Arandiyan, H.; Song, G.; Sun, H.; Sabri, Y.; Zhao, C.; Shao, Z.; Kawi, S. Advancing Catalysts by Stacking Fault Defects for Enhanced Hydrogen Production: A Review. *Adv. Mater.* **2024**, *36* (21), No. 2313378.
(38) Wang, B.; Zhuo, Z.; Li, H.; Liu, S.; Zhao, S.; Zhang, X.; Liu, J.; Xiao, D.; Yang, W.; Yu, H. Stacking Faults Inducing Oxygen Anion Activities in Li_2MnO_3. *Adv. Mater.* **2023**, *35* (22), No. 2207904.
(39) Rani, S.; Roy, S. C.; Bhatnagar, M. C. Effect of Fe Doping on the Gas Sensing Properties of Nano-Crystalline SnO_2 Thin Films. *Sens. Actuators, B* **2007**, *122* (1), 204−210.
(40) Longo, E.; Varela, J. A.; Almeida, D. K. A.; Volanti, D. P. Microwave Aided Device for Hydrothermal Synthesis of Nanostructured Oxides, Particularly Obtaining Particles of Metal Oxides, Comprises Container, in Which Hydrothermal Reaction Takes Place, and Lid for Container. BR200815393-A2, 2010.
(41) Santos, G. S. M.; de Sá, B. S.; Perfecto, T. M.; Volanti, D. P. MOF-Derived Co_3O_4-ZnO Heterostructure for 3-Methyl-1-Butanol Detection. *Sens. Actuators, B* **2024**, *408*, No. 135533.
(42) Oliveira, T. N. T.; Zito, C. A.; Perfecto, T. M.; Azevedo, G. M.; Volanti, D. P. ZnO Twin-Rods Decorated with Pt Nanoparticles for Butanone Detection. *New J. Chem.* **2020**, *44* (36), 15574−15583.
(43) Theodoro, R. d. S.; dos, S.; Sanghikian Marques dos Santos, G.; de Sá, B. S.; Perfecto, T. M.; Volanti, D. P. Multiple-Yolk-Shell NiO Microspheres for Selective Detection of m-Xylene. *ACS Appl. Mater. Interfaces* **2024**, *16* (41), 55637−55649.
(44) Dhanasingh, S.; Nallasamy, D.; Padmanapan, S.; Padaki, V. C. Cetyltrimethylammonium Bromide- and Ethylene Glycol-Assisted Preparation of Mono-Dispersed Indium Oxide Nanoparticles Using Hydrothermal Method. *Chem. Papers* **2014**, *68* (8), 1079−1086.
(45) Yang, J. J.; Cheng, H.; Martens, W. N.; Frost, R. L. Application of Infrared Emission Spectroscopy to the Thermal Transition of Indium Hydroxide to Indium Oxide Nanocubes. *Appl. Spectrosc.* **2011**, *65* (1), 113−118.
(46) Jothibas, M.; Manoharan, C.; Ramalingam, S.; Dhanapandian, S.; Johnson Jeyakumar, S.; Bououdina, M. Preparation, Characterization, Spectroscopic (FT-IR, FT-Raman, UV and Visible) Studies, Optical Properties and Kubo Gap Analysis of In_2O_3 Thin Films. *J. Mol. Struct.* **2013**, *1049*, 239−249.
(47) Sing, K. S. W.; Everett, D. H.; Haul, R. A. W.; Moscou, L.; Pierotti, R. A.; Rouquérol, J.; Siemieniewska, T. Reporting Physisorption Data for Gas/Solid Systems with Special Reference to the Determination of Surface Area and Porosity. *Pure Appl. Chem.* **1985**, *57* (4), 603−619.
(48) Zhang, Q.; Wang, S.; Fu, H.; Wang, Y.; Yu, K.; Wang, L. Facile Design and Hydrothermal Synthesis of In_2O_3 Nanocube Polycrystals with Superior Triethylamine Sensing Properties. *ACS Omega* **2020**, *5* (20), 11466−11472.
(49) Walker, J. M.; Akbar, S. A.; Morris, P. A. Synergistic Effects in Gas Sensing Semiconducting Oxide Nano-Heterostructures: A Review. *Sens. Actuators, B* **2019**, *286*, 624−640.
(50) Yang, Y.; Shen, C.; Sun, K.; Mei, D.; Liu, C. J. Enhanced Surface Charge Localization Over Nitrogen-Doped In_2O_3 for CO_2 Hydrogenation to Methanol with Improved Stability. *ACS Catal.* **2023**, *13* (9), 6154−6168.
(51) Al-Hashem, M.; Akbar, S.; Morris, P. Role of Oxygen Vacancies in Nanostructured Metal-Oxide Gas Sensors: A Review. *Sens. Actuators, B* **2019**, *301*, No. 126845.
(52) Shifu, C.; Xiaoling, Y.; Huaye, Z.; Wei, L. Preparation, Characterization and Activity Evaluation of Heterostructure In_2O_3/$In(OH)_3$ Photocatalyst. *J. Hazard Mater.* **2010**, *180* (1−3), 735−740.
(53) Shanmuga Priya, B.; Shanthi, M.; Manoharan, C.; Bououdina, M. Hydrothermal Synthesis of Ga-Doped In_2O_3 Nanostructure and Its Structural, Optical and Photocatalytic Properties. *Mater. Sci. Semicond. Process.* **2017**, *71*, 357−365.
(54) Kortüm, G. *Reflectance Spectroscopy*; Springer Berlin Heidelberg: Berlin, Heidelberg, 1969. DOI: 10.1007/978-3-642-88071-1.
(55) Senthilkumar, V.; Vickraman, P.; Ravikumar, R. Synthesis of Fluorine Doped Tin Oxide Nanoparticles by Sol-Gel Technique and Their Characterization. *J. Solgel Sci. Technol.* **2010**, *53* (2), 316−321.
(56) Walsh, A.; Catlow, C. R. A.; Zhang, K. H. L.; Egdell, R. G. Control of the Band-Gap States of Metal Oxides by the Application of Epitaxial Strain: The Case of Indium Oxide. *Phys. Rev. B Condens Matter Mater. Phys.* **2011**, *83* (16), No. 161202.
(57) Chen, Y.; Zhou, X.; Zhao, X.; He, X.; Gu, X. Crystallite Structure, Surface Morphology and Optical Properties of In_2O_3−TiO_2 Composite Thin Films by Sol−Gel Method. *Mater. Sci. Eng.: B* **2008**, *151* (2), 179−186.
(58) Yamazoe, N.; Sakai, G.; Shimanoe, K. Oxide Semiconductor Gas Sensors. *Catal. Surv. Asia* **2003**, *7* (1), 63−75.
(59) Pavelko, R. G.; Daly, H.; Hardacre, C.; Vasiliev, A. A.; Llobet, E. Interaction of Water, Hydrogen and Their Mixtures with SnO_2 Based Materials: The Role of Surface Hydroxyl Groups in Detection Mechanisms. *Phys. Chem. Chem. Phys.* **2010**, *12* (11), 2639−2647.
(60) Jin, Z.; Zhao, J.; Liu, L.; Liu, F.; Wang, Z.; Wang, F.; Liu, J.; Mou, Y.; Wu, L.; Wu, X. Humidity-Independent Gas Sensors in the Detection of Hydrogen Sulfide Based on Nd_2O_3-Loaded In_2O_3 Porous Nanorods. *Sens. Actuators, B* **2024**, *403*, No. 135237.
(61) Shen, J.; Li, F.; Yin, B.; Sun, L.; Chen, C.; Wen, S.; Chen, Y.; Ruan, S. Enhanced Ethyl Acetate Sensing Performance of Al-Doped In_2O_3 Microcubes. *Sens. Actuators, B* **2017**, *253*, 461−469.
(62) Liu, N.; Wang, X. F.; Zhang, G.; Liang, H.; Li, T.; Zhao, Y.; Zhang, T.; Tan, Z.; Song, X. Z. Metal-Organic Framework-Derived Porous $NiFe_2O_4$ Nanoboxes for Ethyl Acetate Gas Sensors. *ACS Appl. Nano Mater.* **2022**, *5* (10), 14320−14327.
(63) Xie, X.; Wang, X.; Tian, J.; Liu, J.; Cao, H.; Song, X.; Wei, N.; Cui, H. Facile Synthesis and Superior Ethyl Acetate Sensing Performance of Au Decorated ZnO Flower-like Architectures. *Ceram. Int.* **2017**, *43* (6), 5053−5060.

(64) Fan, Y.; Wang, W.; Zhang, J.; Lu, Y.; Liu, C.; Adimi, S.; Zhou, J.; Ruan, S.; Chen, Y. Construction of P-n Heterojunctions by Modifying MOF-Derived α-Fe_2O_3 with Partially Covered Cobalt Tungstate for High-Performance Ethyl Acetate Detection. *Sens. Actuators, B* **2021**, *344*, No. 130129.
(65) Yin, Y.; Zhang, N.; Han, J.; Liu, C.; Adimi, S.; Wen, S.; Li, X.; Ruan, S. Metal-Organic Framework Derived Core-Shell $PrFeO_3$-Functionalized α-Fe_2O_3 Nano-Octahedrons as High Performance Ethyl Acetate Sensors. *Sens. Actuators, B* **2019**, *297*, No. 126738.

https://doi.org/10.1021/acsanm.5c01487
ACS Appl. Nano Mater. 2025, 8, 11458−11469